swarm Data, Innovation, and Science Cluster SWARM DISC

Validation Report

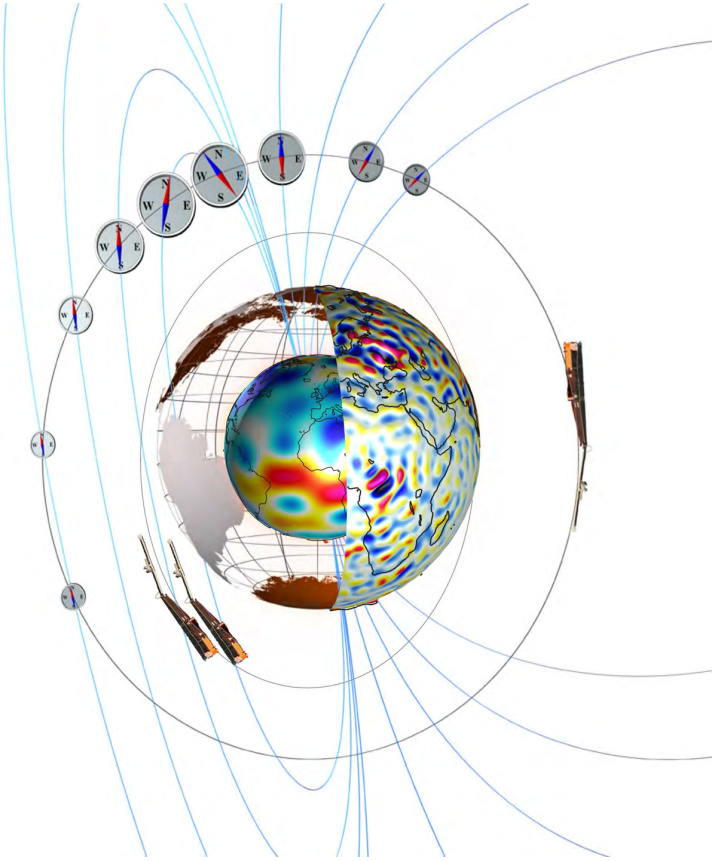

Doc.No: SW-TN-BCSS-GS-0004, Rev: 1A

Prepared:

Karl Magnus Laundal — Date 2018–06–21
Project Manager

Prepared:

Jone Reistad — Date 2018–06–21
Project Scientist

Approved:

Date 2018–06–21

Checked:

Date 2018–06–21

Record of changes

Reason	Description	Rev	Date
Issue 1	draft A	1 dA	2018-06-15

Table of Contents

Preface

This document reports comparisons of estimates of ionospheric magnetic field disturbances and current densities from the Average Magnetic field and Polar current System (AMPS) model with various measurements: Swarm magnetic field data, from a period after the last data point used in the model (Section 1); Ørsted magnetic field measurements (Section 2); and field-aligned current (FAC) estimates by the Active Magnetosphere and Planetary Electrodynamics Response Experiment (AMPERE, Section 3). In addition, we show comparisons with the Swarm L2 dual satellite field-aligned current data product (Section 4) and with ground magnetic field measurements (Section 5).

The main purpose of these comparisons is to confirm that the AMPS model describes the large-scale average magnetic field disturbances and associated current densities in low Earth orbit. However, we also present comparisons with small-scale FACs and with ground perturbations, in order to highlight differences and potential additional uses of the AMPS model.

The emphasis of this report is on the graphics presenting quantitative comparisons. Discussions of potential explanations for observed differences are presented only briefly in this report, since they are subject to active research.

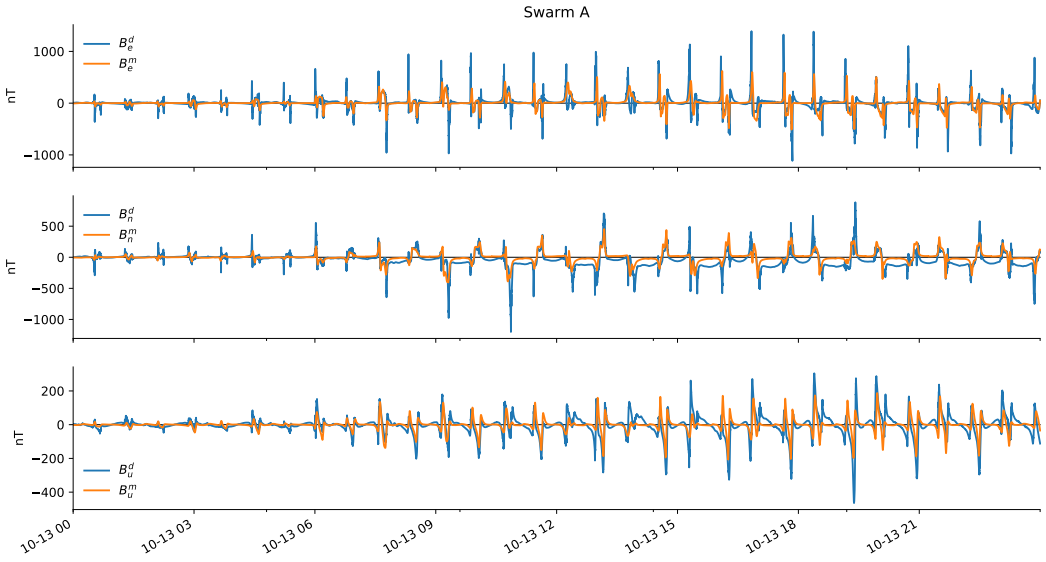

Figure 1: One day of measurements of the magnetic field minus CHAOS estimates of core and crustal magnetic fields, and AMPS model predictions of the ionospheric disturbance magnetic field along the Swarm Alpha orbit. Superscripts d and m indicate data and model, respectively. Subscripts e, n, and u indicate components in the east, north, and up directions, respectively. The date is 13 October 2016.

1 Comparison with independent Swarm data

In this section we compare AMPS estimates of the magnetic field to magnetic field measurements form Swarm Alpha and Bravo, taken from September 2016 to August 2017. This period was not included in the dataset used to make the model.

The magnetic field measurements and model estimates were downloaded from VirES. CHAOS-6 model estimates of the core and crustal magnetic fields were subtracted from the measured magnetic field. Model estimates of magnetospheric fields were not available from VirES at the time when the dataset was made, so it was *not* subtracted. This makes the comparison with AMPS model predictions biased, since the data used to make the AMPS model were corrected for large-scale magnetospheric field contributions. We expect this to give the largest deviations at lower latitudes, so we concentrate on Quasi-Dipole (QD) latitudes poleward of $\pm 50°$.

Figures 1 and 2 show one day of measurements and model estimates from Alpha and Bravo, respectively. We see that model estimates largely reproduce the shape of the disturbance field as the satellite crosses polar regions. The amplitudes of the model perturbations are, according to visual inspection, well correlated, but systematically lower than the amplitude of the measurement residuals.

Results of a more quantitative analysis are presented in Figures 3 and 4, based on data from Swarm Alpha and Bravo, respectively. The top panels in these figures show the root-mean-square (RMS) of the data and error (data − AMPS model predictions), in three different components, as functions of QD latitude. The RMS is calculated robustly, using iterative reweighting by Huber

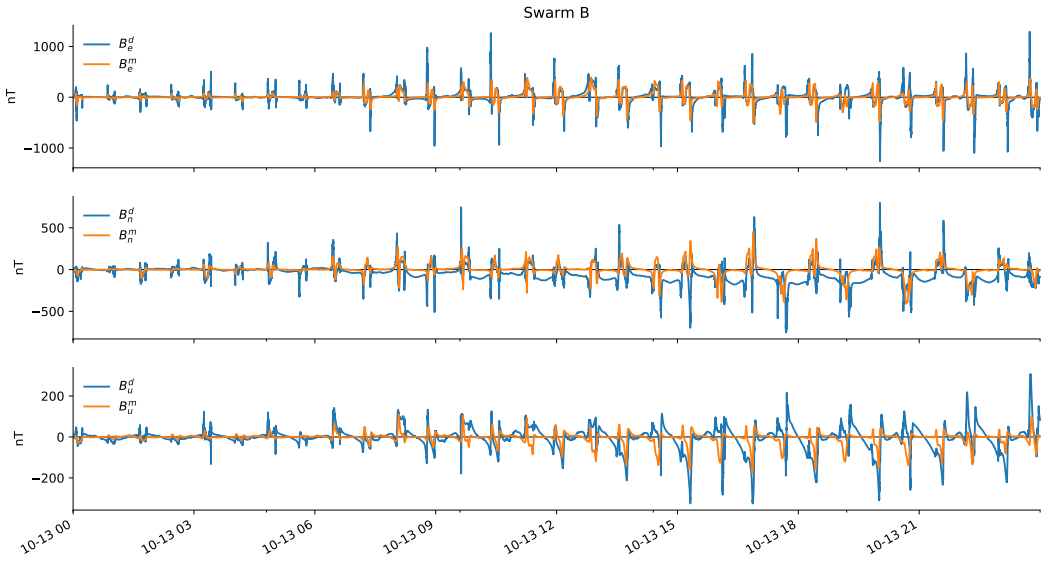

Figure 2: One day of measurements of the magnetic field minus CHAOS estimates of core and crustal magnetic fields, and AMPS model predictions of the ionospheric disturbance magnetic field along the Swarm Bravo orbit. Superscripts d and m indicate data and model, respectively. Subscripts e, n, and u indicate components in the east, north, and up directions, respectively. The date is 13 October 2016.

weights. The procedure is the same that was used with Ørsted data in the model paper [Laundal et al., 2018], see also Section 2.

The lower panels show the prediction efficiency, calculated as $1 - \mathrm{var}(\mathbf{e})/\mathrm{var}(\mathbf{d})$, where $\mathbf{e}$ and $\mathbf{d}$ are arrays of residuals and data points, respectively. The variance is also calculated robustly with Huber weights. The prediction efficiency indicates how well the model predicts the measurements: A value of 1 indicates perfect prediction, and a value of 0 indicates a performance similar to using just the mean value. Negative values mean that the model invents a non-existent signal, doing more harm than good. We see a clear dependence on latitude in the prediction efficiency, with higher values towards the poles. The signal itself maximizes in the auroral zone, near $\pm 70°$. Equatorward of this the prediction efficiency decreases. The prediction efficiency in the upward component reaches negative values near the equatorward edge of the aurora zone.

Figures 1 and 2 show that there is a clear mismatch in baselines, most notably in the northward component. This is likely an effect of the missing magnetospheric correction in the data that we use here. This is probably a major reason for the negative prediction efficiencies seen at lower latitudes in Figures 3 and 4, and a contributing factor to the overall reduction in prediction efficiency with decreasing latitude. We discuss this further in the next section, where we compare with Ørsted data.

2 Comparison with Ørsted data

In this section we compare model estimates of the magnetic field to measurements from the Ørsted satellite. The Ørsted measurements predate the first data point used when making the model, from CHAMP, between March 1999 and July 2000. The preprocessing of the Ørsted data was the same as with the Swarm and CHAMP data used to make the model: 30 s sampling, and subtraction of core, crust, and magnetospheric magnetic fields.

Figures 5, 6, and 7 show the result of comparisons between AMPS model estimates of magnetic field and Ørsted data taken during quiet, moderate, and active conditions, respectively. The level of geomagnetic conditions was determined using the Kp index, with bins defined by

$$\text{quiet} \leq 3_0 < \text{moderate} < 4_0 \leq \text{active}. \tag{1}$$

The format of the figures is the same as in Figures 3 and 4. It is also the same as Figure 3 of Laundal et al. [2018], which is based on the same data set but without any separation by geomagnetic activity.

The Ørsted comparisons have a similar pattern as the comparisons with Swarm alpha and bravo meaurements in the previous section. The most notable exception is in the upward component, which is generally smaller in Ørsted. The reason for this is probably that Ørsted was in a higher orbit, and the upward component is most sensitive to horizontal currents below, whose magnetic effect diminishes with height.

It is interesting to note that the prediction efficiency in the upward component is consistently higher in Ørsted than in the Swarm comparisons. This may also be an effect of the different heights, with Ørsted being less sensitive to variations in small-scale structures than Swarm.

We also notice a pattern in the prediction efficiency in the upward component, which, on close inspection, is consistent with all the plots on this format: Approximately at $65 - 70°$, the prediction efficiency makes a sharp drop, and then recovers to follow the smoother trend of reduced prediction efficiency towards lower latitudes. We speculate that this is because of variabilities in the westward electrojet associated with substorms. Substorms can produce a very strong signal, which is not parametrized in the current version of the model.

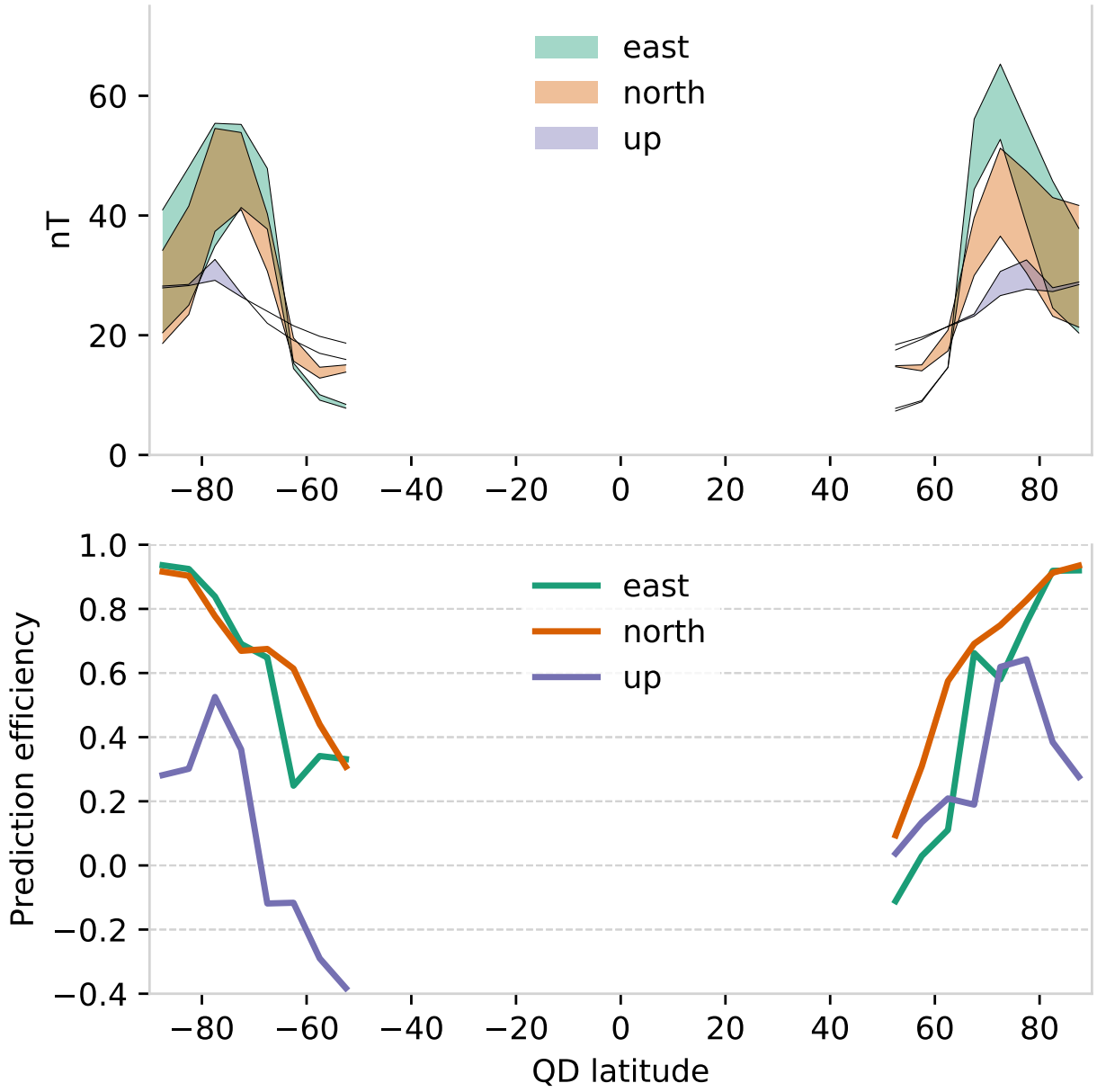

Figure 3: Top: The root-mean-square (RMS) data and data-model residuals in bins of 5° QD latitude, for three components of the magnetic field. The colored regions indicate where the RMS residual is lower than the RMS of the data. The RMS is calculated robustly, with iteratively reweighting by Huber weights. Bottom: The prediction efficiency, calculated using the same data as in the top plot. This figure is based on data from Swarm Alpha from a period after the last datapoint in the AMPS model (see text for details).

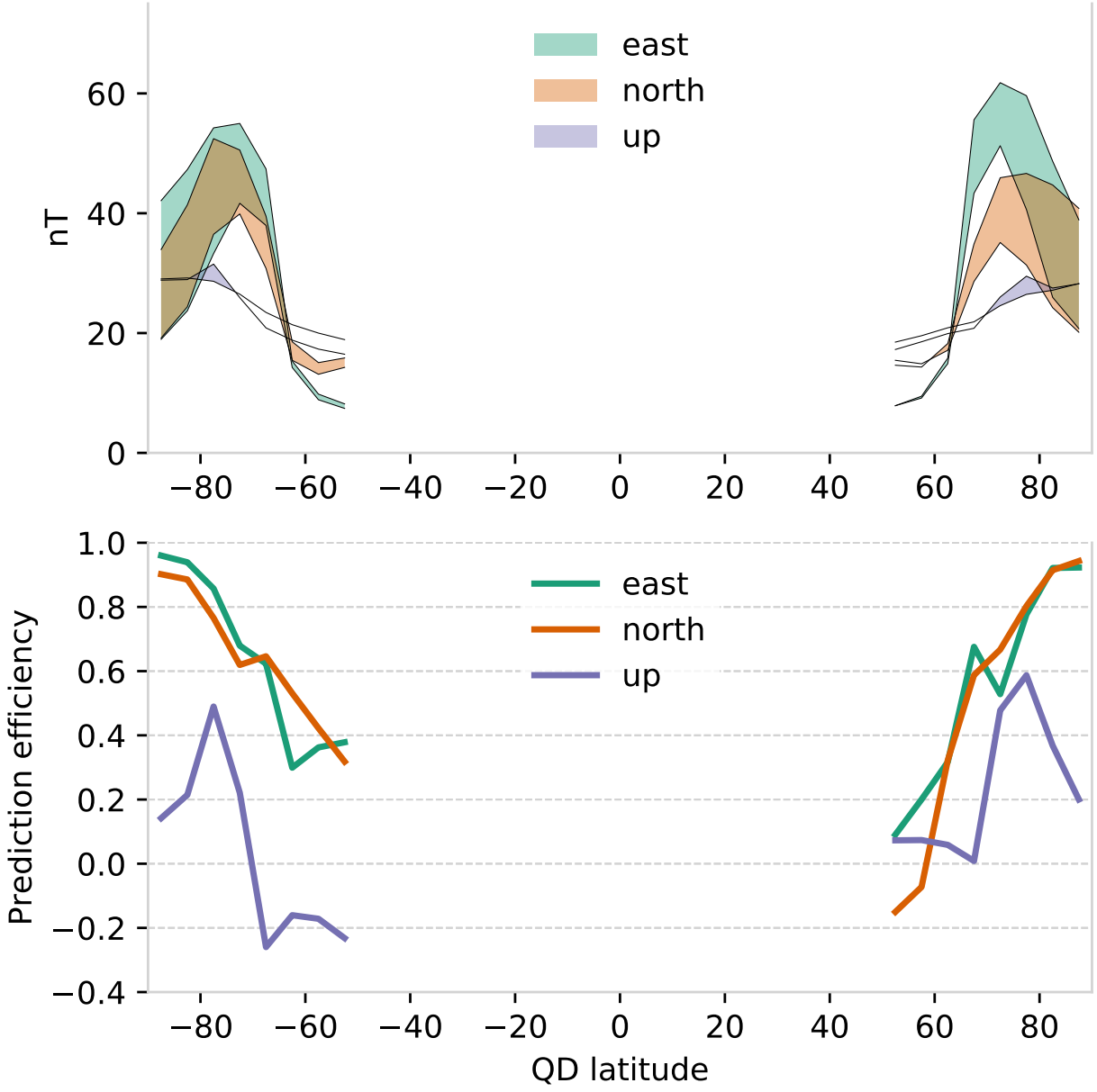

Figure 4: This figure is based on data from Swarm Bravo from a period after the last datapoint in the AMPS model (see text for details). Otherwise the format is the same as in Figure 3.

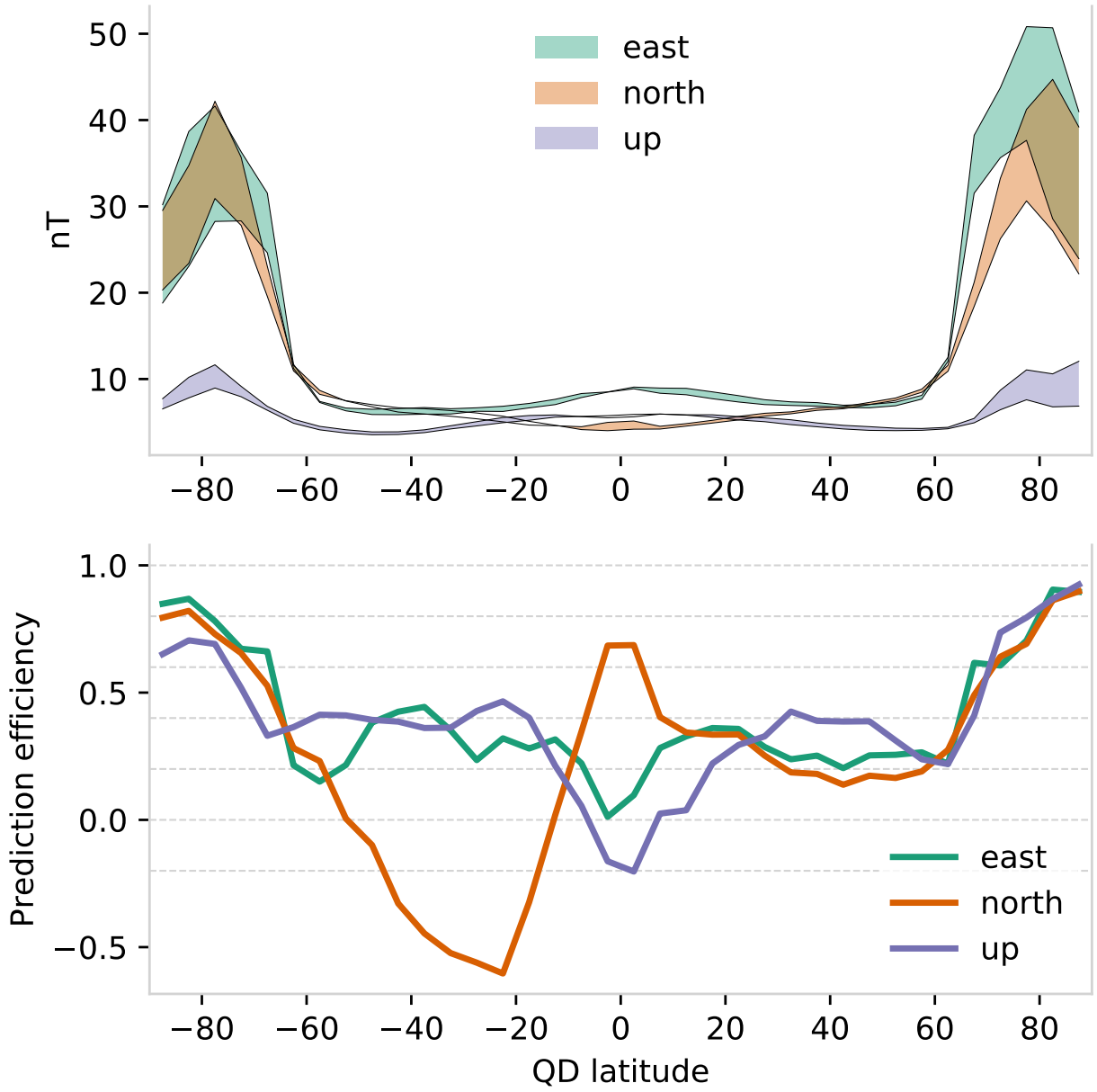

Figure 5: This figure is based on data from Ørsted from a period before the first datapoint used to make the AMPS model (see text for details), during times when Kp $\leq 3_0$ (relatively quiet). Otherwise the format is the same as in Figure 3.

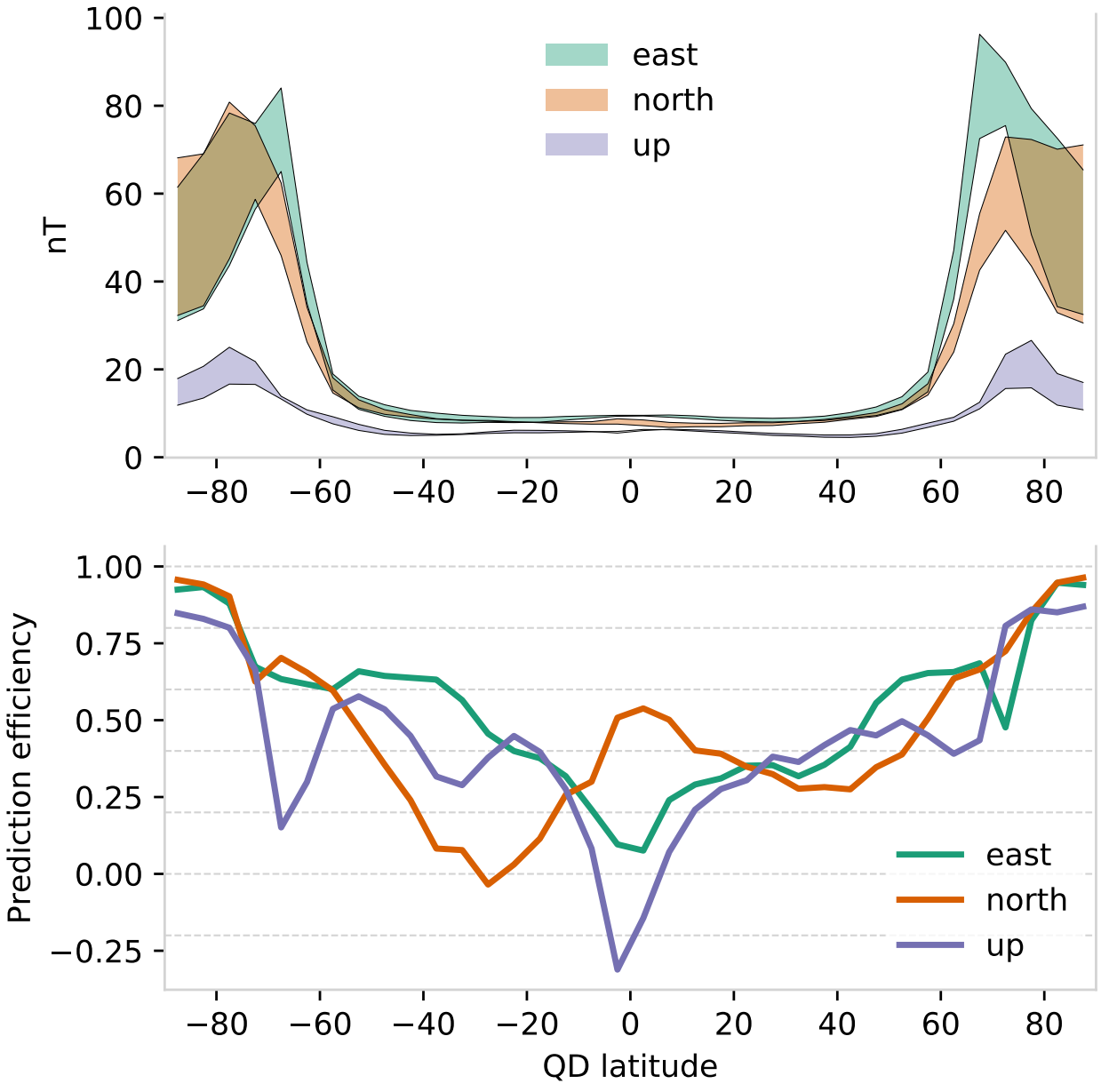

Figure 6: This figure is based on data from Ørsted from a period before the first datapoint used to make the AMPS model (see text for details), during times when $3_0 < \mathrm{Kp} < 4_0$ (moderate geomagnetic activity). Otherwise the format is the same as in Figure 3.

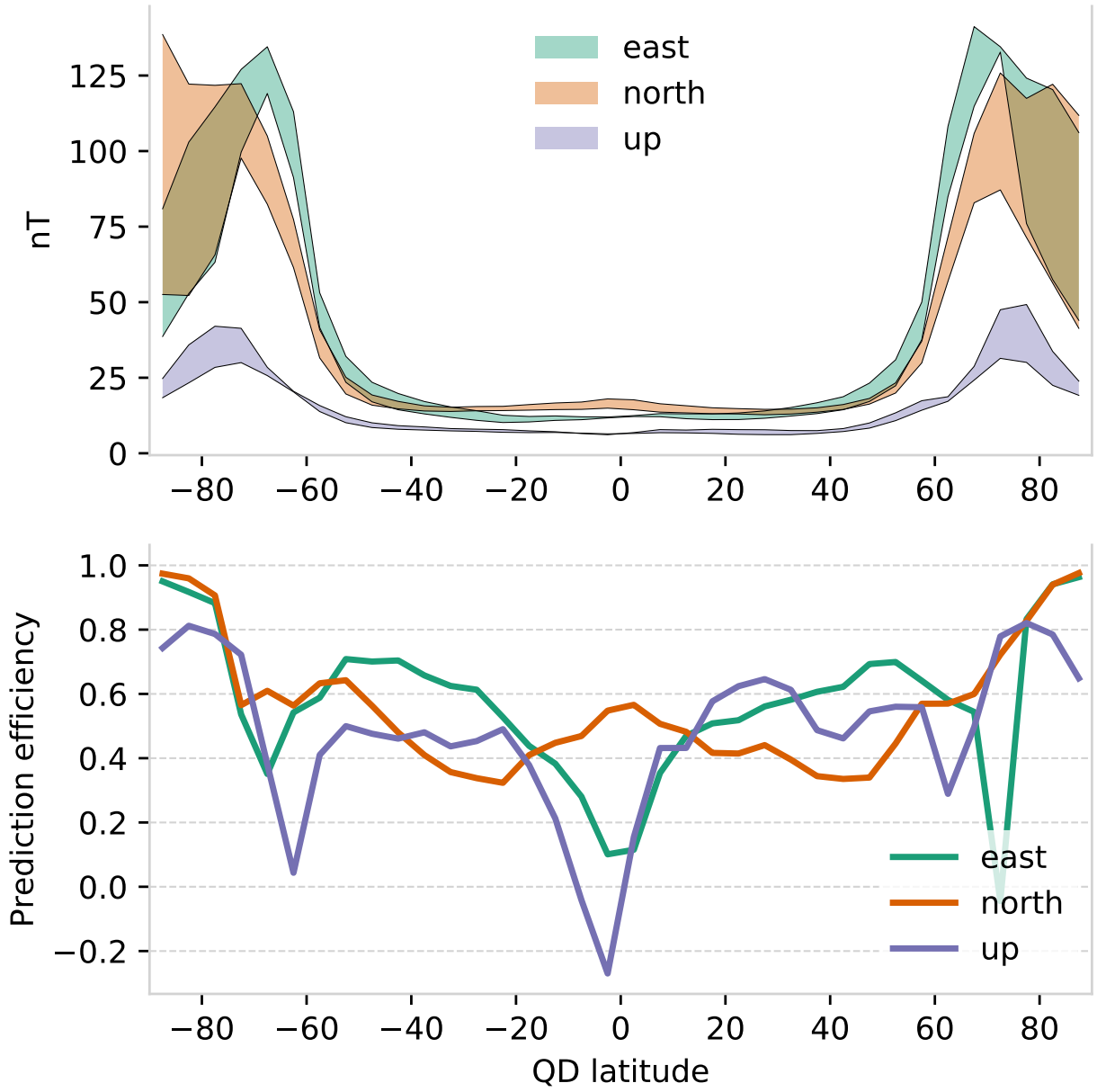

Figure 7: This figure is based on data from Ørsted from a period before the first datapoint used to make the AMPS model (see text for details), during times when Kp $\geq 4_0$ (active geomagnetic conditions). Otherwise the format is the same as in Figure 3.

3 Comparison with AMPERE

In this section we compare AMPS model estimates of the field-aligned current (FAC) to estimates from the Active Magnetosphere and Planetary Electrodynamics Response Experiment (AMPERE, Waters et al. [2001], Anderson et al. [2000, 2017])[1]. AMPERE uses 10 min of magnetic field measurements from 66 Iridium satellites to estimate polar maps of FACs in both hemispheres. These maps are available at 2 min cadence, since 2010. The comparisons between AMPS and AMPERE are divided in two sections: First we compare temporal averages of the total integrated currents, and then we compare AMPS model FAC maps with average AMPERE FACs during similar external conditions.

3.1 Total current

Figure 8 is from an ongoing study of north-south asymmetries in current system. Its format is inspired by Coxon et al. [2016], who investigated north-south asymmetries in currents estimated by AMPERE. They found that in general, the currents are stronger in the northern hemisphere than they are in the southern hemisphere. We have repeated their analysis, with both AMPERE and AMPS, and present the results here for the purpose of validation.

The figure shows time series of total upward current in (top) AMPERE and AMPS, shown as transparent and opaque curves, respectively, with the northern hemisphere in blue and southern hemisphere in red. The values are 27 days averages, and the number on the x axis indicates the Bartels rotation number (number of 27 day periods, close the rotation period of the Sun as it appears from Earth, since 8 February 1832). When calculating the integrated AMPERE current, current densities less than $0.2\mu\mathrm{A/m}^2$ were assumed to be noise and ignored, following Coxon et al. [2016]. We see that the resulting integrated current magnitudes are very similar with AMPERE and AMPS.

The bottom panel in Figure 8 shows the difference in total current between the northern and southern hemisphere. A clear annual variation is seen in the difference. In AMPERE, this annual variation is slightly larger than in AMPS. The dominant contribution to the annual variation is seasonal variations in the conductivity, but Coxon et al. [2016] pointed out that an additional contribution comes from a serendipitous variation in the solar wind driving. The solar wind driving is summarized by the coupling function by Milan et al. [2012], shown in the second panel. This coupling function reflects the dayside reconnection rate, and its unit is kV. To compensate for the serendipitous variation in dayside reconnection rate, Coxon et al. [2016] considered a global Ohm's law, in which the total current is expressed as a global conductivity times the dayside reconnection rate. The global conductivity was expressed as a constant plus a sinusoidal function in phase with seasons. By using the measurements of current and reconnection electric potential, the amplitude of the global conductivity can be fitted.

Table 1 shows the amplitudes that we find with AMPERE and AMPS. It shows, in agreement with Coxon et al. [2016], that the conductivities are larger in the northern hemisphere when we use AMPERE. With AMPS, the differences are small, and not statistically significant.

In conclusion, we find that AMPS and AMPERE give similar magnitudes for the total upward field-aligned currents. A more careful analysis reveals that the north-south asymmetry observed with AMPERE is not present in AMPS. One possible reason for the north-south asymmetries in AMPERE is the different data distributions in the two hemispheres, with the orbital planes of the Iridium satellites intersecting at lower magnetic latitudes in the south than in the north. With

[1] http://ampere.jhuapl.edu/

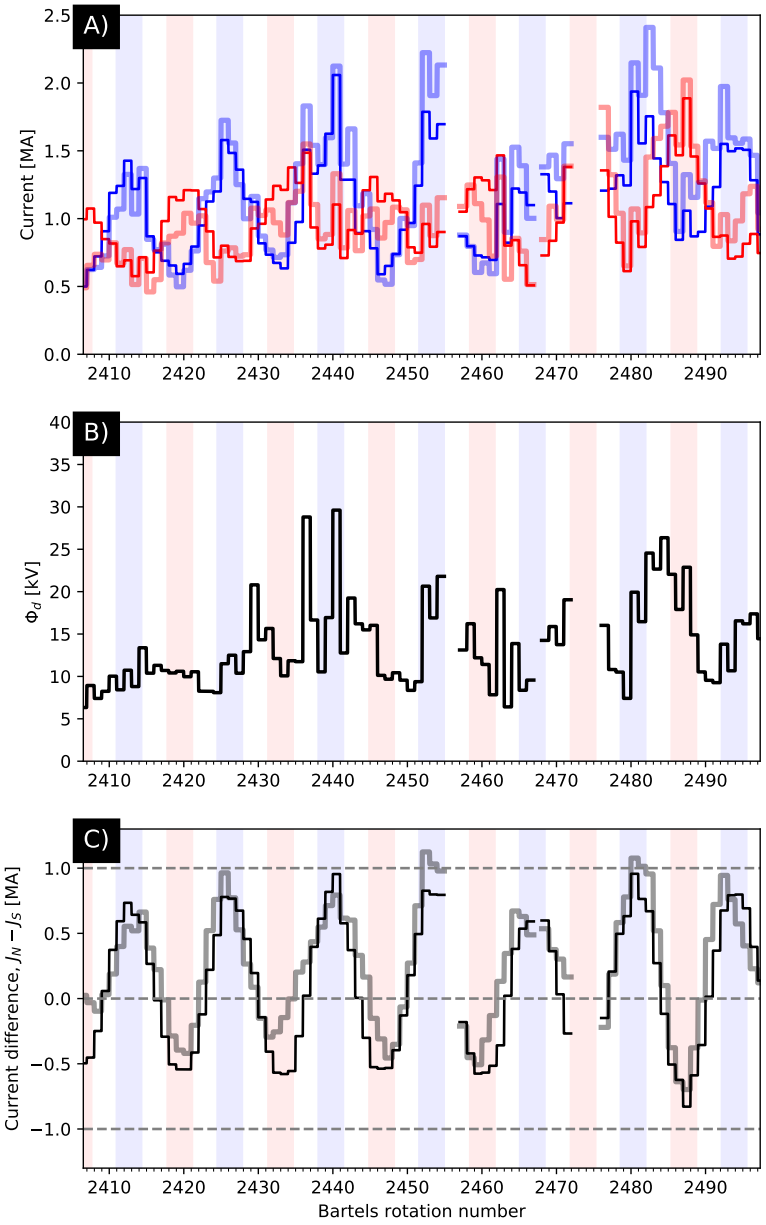

Figure 8: Time series of (top) total upward current derived with AMPERE (transparent) and AMPS (opaque) in the northern (blue) and southern (red) hemispheres; (middle) dayside reconnection rate; and (bottom) the difference in total current between the northern and southern hemispheres. Each datapoint represents a 27 day average, and the time axis is labeled by Bartels rotation number. The format is derived from Figure 2 in Coxon et al. [2016].

Table 1: The global conductivity parameter, estimated with total currents from the AMPS model and from AMPERE, and the magnetopause reconnection rate using the coupling function by Milan et al. [2012]. The conductivity parameter varies with seasons, and t indicates time since spring equinox, normalized so that $t = 2\pi$ after one year.

Σ_N^{AMPS}	=	73.31(±4.35)	+	24.00(±6.32)	$\sin(t)$
Σ_S^{AMPS}	=	69.39(±3.85)	−	24.51(±5.59)	$\sin(t)$
Σ_N^{AMPERE}	=	84.50(±4.84)	+	24.95(±7.03)	$\sin(t)$
Σ_S^{AMPERE}	=	70.98(±3.26)	−	15.04(±4.73)	$\sin(t)$

the AMPS model, we do not have this bias. The confirmation of this speculation requires a more careful analysis, and is beyond the scope of this report.

3.2 Spatial maps

In this section we present comparisons of statistical maps of Birkeland current densities made using AMPS with statistical maps made with AMPERE. We reproduce the clock angle plots presented in Laundal et al. [2018], in Figures 5, 6, and 7, without the divergence-free current, and plot comparable average maps from AMPERE on top. We also present corresponding figures from the southern hemisphere. The AMPERE maps were made by calculating the average in bins defined by selecting IMF $|B| \in [2.5, 5.5]$ (unit nT), velocity $v \in [300, 400]$ (unit km/s), tilt either $\leq -15°$, $\in [-10°, 10°]$, or $\geq 15°$, and clock angle in 45° wide bins centered on the value used for the corresponding AMPS calculation. The binned averages are calculated robustly, using iterative reweighting by Huber weights. The AMPERE data covers the period from 2010 to 2013.

The results are shown in Figures 9−14. The filled contours show the AMPS model FACs, and the black contours show FACs based on AMPERE. The main conclusion from these figures is that the two sets of average FACs are very similar. Subtle differences are present, but also expected, since the AMPERE bins only approximately correspond to the external conditions used with the AMPS model.

4 Comparison with *Swarm* AC FAC estimates

We have made a comparison of the AMPS model field-aligned current with the field-aligned current densities derived with the dual spacecraft approach using Swarm Alpha and Charlie. The L2 FAC data product is an estimate of the instantaneous FAC along the satellite orbits [Ritter et al., 2013], while the AMPS model provides the large-scale average FAC. The correspondence between the current densities at these different spatial and temporal scales is not trivial and still an area of active research [McGranaghan et al., 2017]. The comparison presented below highlights this.

An example time series is shown in Figure 15, covering two crossings of the auroral zones. Dual-satellite estimates are shown in black, and AMPS estimates in orange. Clearly the dual satellite estimates show small-scale structure that is not reflected in AMPS. The fit in Figure 15 is better than many other crossings, which often show multiple strong peaks in the dual-satellite FACs, and peaks that are offset with respect to the large-scale pattern in AMPS.

For each day between 15 April 2014 and 30 December 2016 we calculate the following statistics: The correlation between the dual satellite FAC and the AMPS FAC estimates; the prediction efficiency, a measure of how well AMPS predicts the dual satellite FAC; and the slope in a simple linear regression model, without intersect, of AMPS FAC as function of dual satellite FAC estimate.

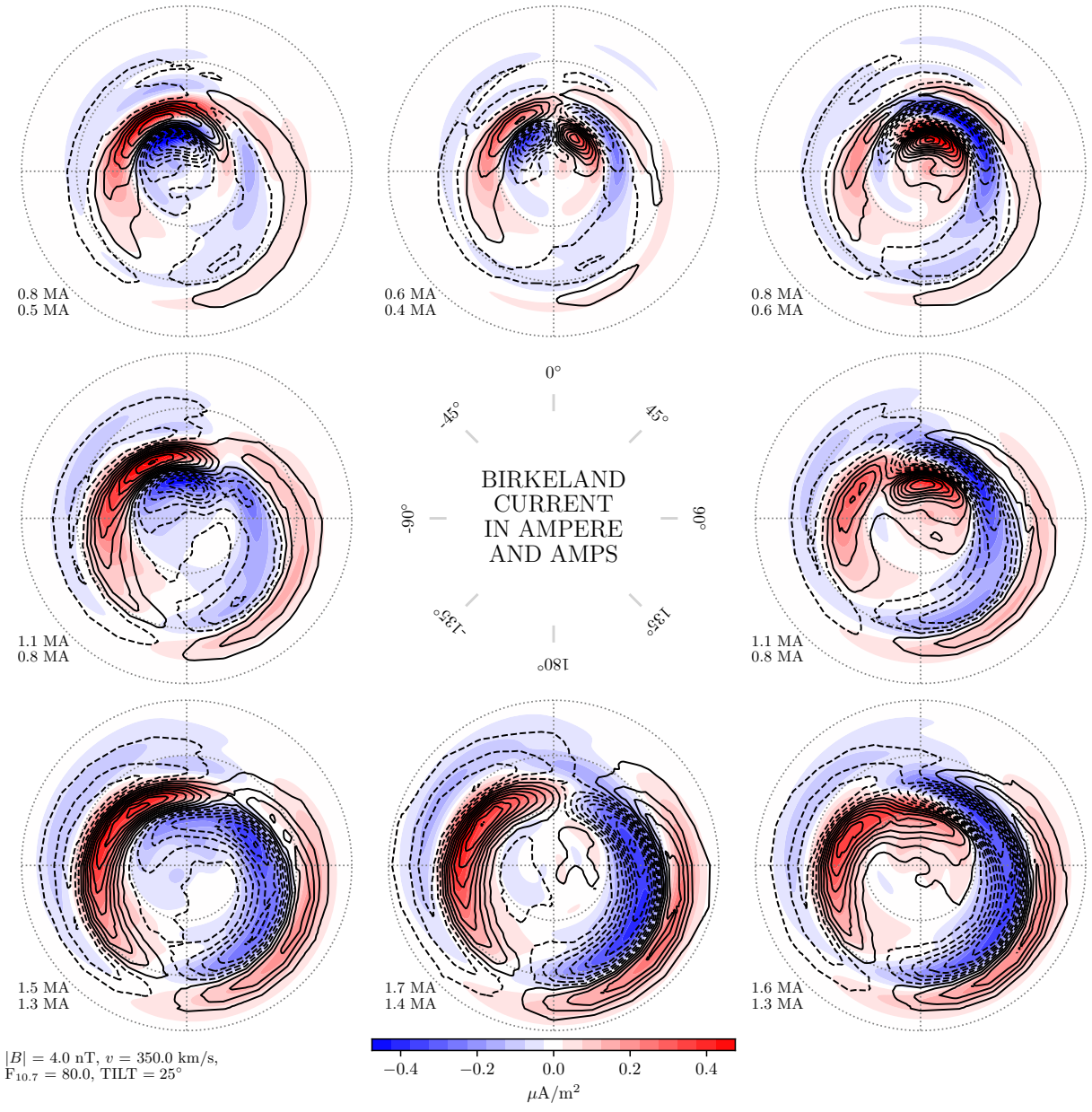

Figure 9: Maps of field-aligned current densities from the AMPS model (filled contours), for external conditions indicated in the lower left corner, and IMF orientation indicated in the center. The black contours show field-aligned current densities estimated with AMPERE, using bins defined by external conditions similar to values used with the AMPS model. The contour spacing is the same as in the filled contours, and dashed lines indicate negative (downward) current densities. The numbers in the lower left corners of each map shows the total upward current in AMPS (top) and AMPERE (bottom), in units of MA. The unit is given by the color scale below the maps. This plot corresponds to **summer** conditions (positive tilt) in the **north**ern hemisphere.

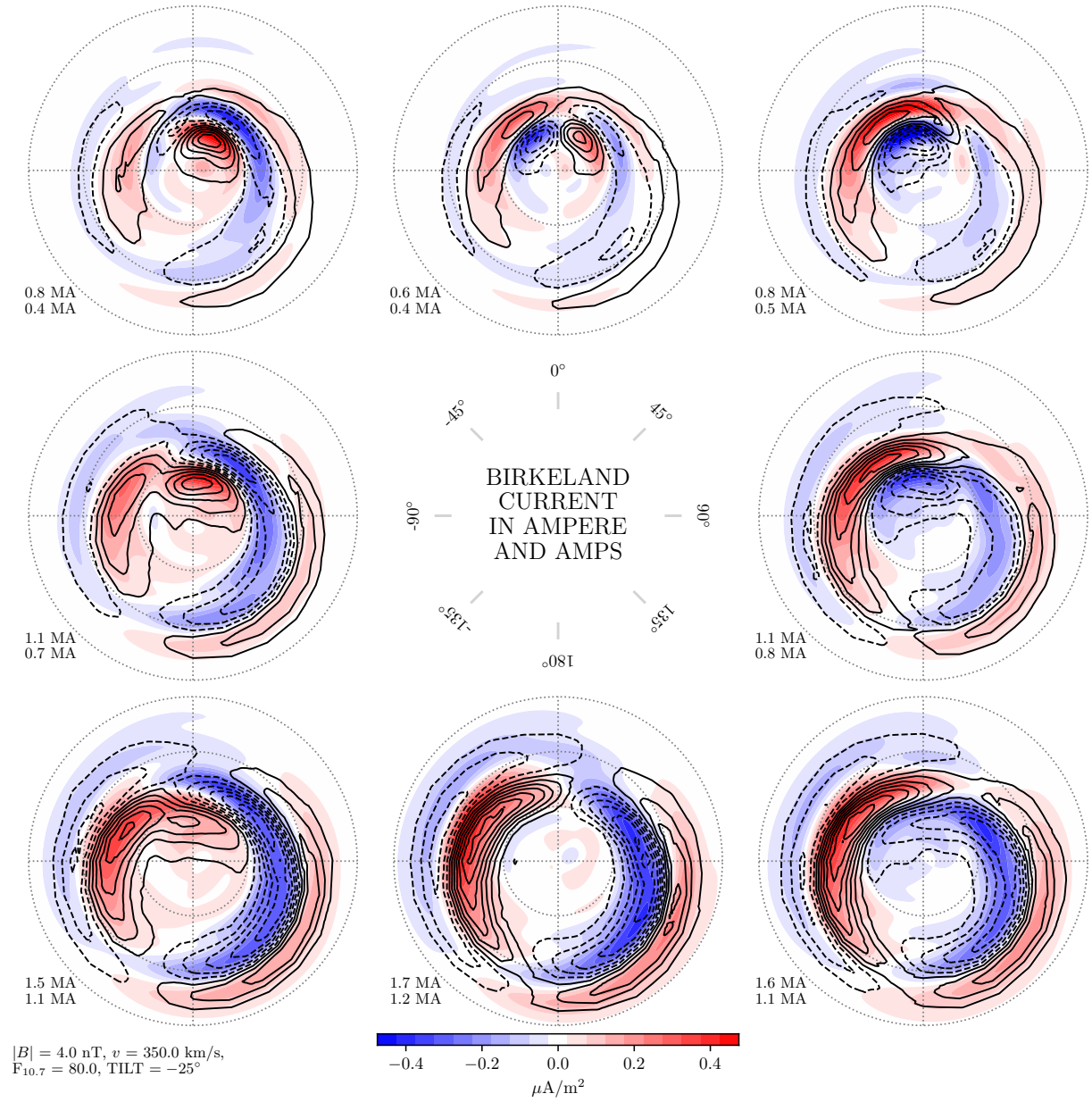

Figure 10: Maps of field-aligned current densities from the AMPS model (filled contours), for external conditions indicated in the lower left corner, and IMF orientation indicated in the center. The black contours show field-aligned current densities estimated with AMPERE, using bins defined by external conditions similar to values used with the AMPS model. The contour spacing is the same as in the filled contours, and dashed lines indicate negative (downward) current densities. The numbers in the lower left corners of each map shows the total upward current in AMPS (top) and AMPERE (bottom), in units of MA. The unit is given by the color scale below the maps. This plot corresponds to **summer** conditions (positive tilt) in the **south**ern hemisphere.

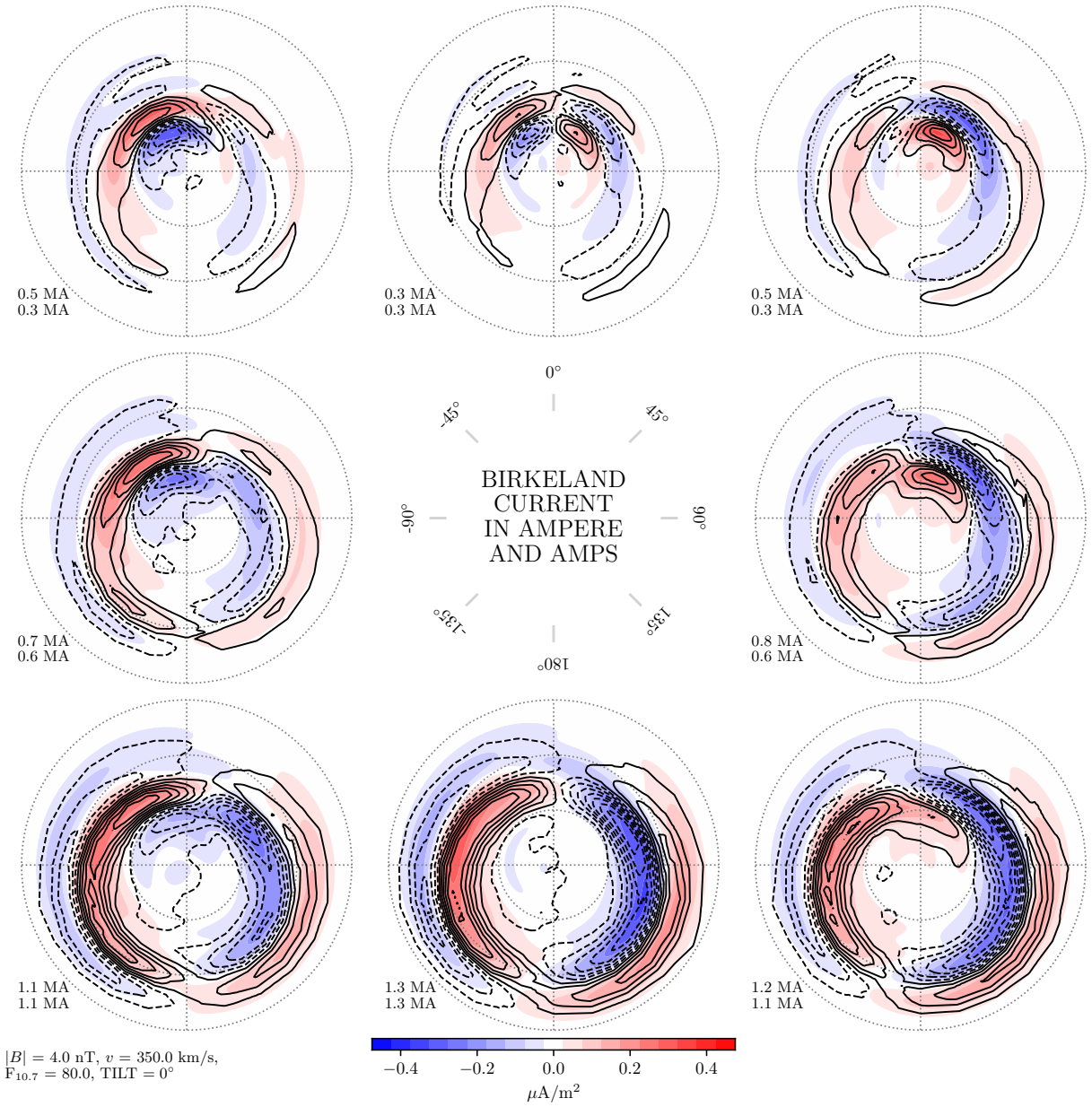

Figure 11: Maps of field-aligned current densities from the AMPS model (filled contours), for external conditions indicated in the lower left corner, and IMF orientation indicated in the center. The black contours show field-aligned current densities estimated with AMPERE, using bins defined by external conditions similar to values used with the AMPS model. The contour spacing is the same as in the filled contours, and dashed lines indicate negative (downward) current densities. The numbers in the lower left corners of each map shows the total upward current in AMPS (top) and AMPERE (bottom), in units of MA. The unit is given by the color scale below the maps. This plot corresponds to **equinox** conditions (positive tilt) in the **north**ern hemisphere.

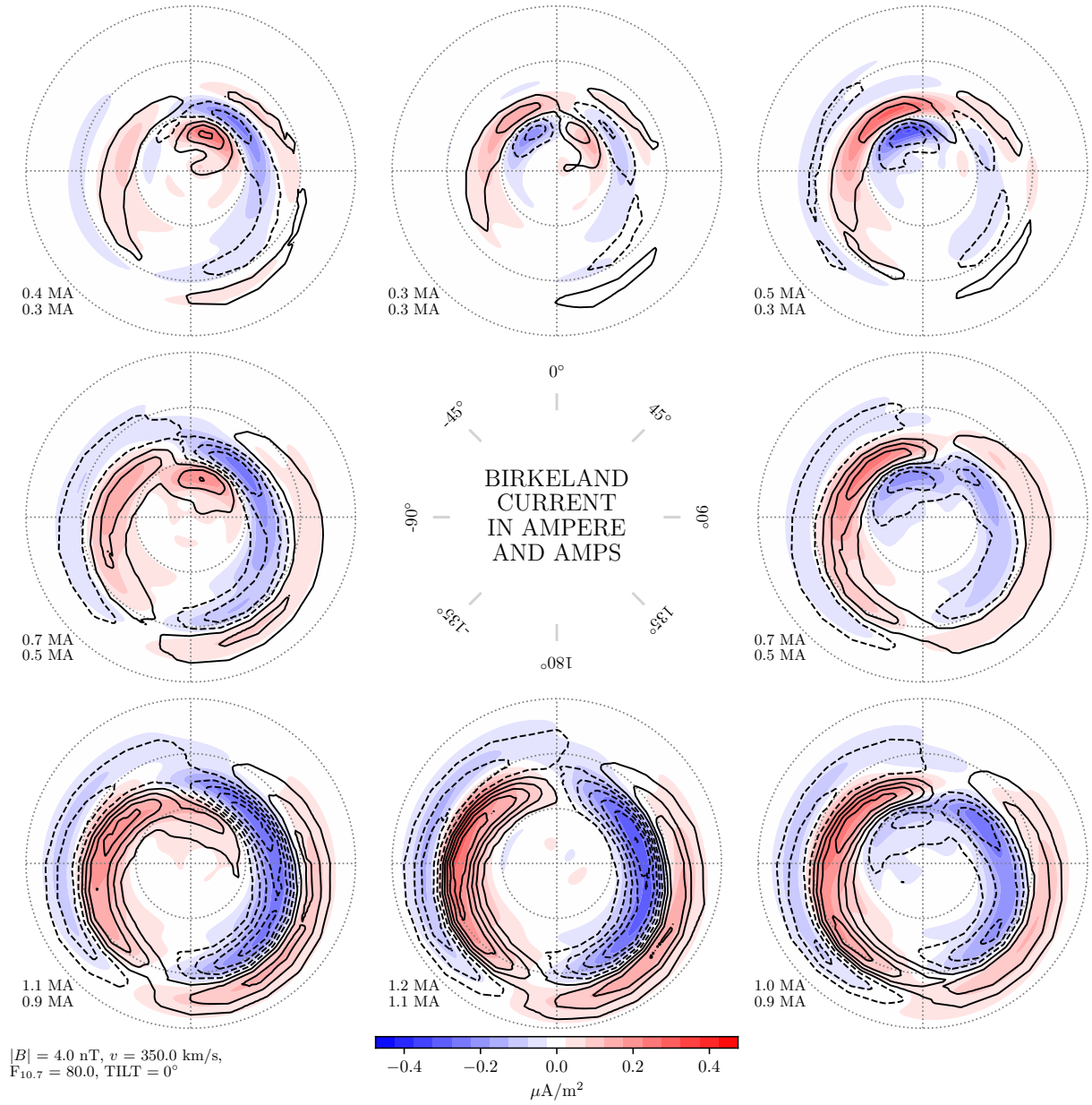

Figure 12: Maps of field-aligned current densities from the AMPS model (filled contours), for external conditions indicated in the lower left corner, and IMF orientation indicated in the center. The black contours show field-aligned current densities estimated with AMPERE, using bins defined by external conditions similar to values used with the AMPS model. The contour spacing is the same as in the filled contours, and dashed lines indicate negative (downward) current densities. The numbers in the lower left corners of each map shows the total upward current in AMPS (top) and AMPERE (bottom), in units of MA. The unit is given by the color scale below the maps. This plot corresponds to **equinox** conditions (positive tilt) in the **south**ern hemisphere.

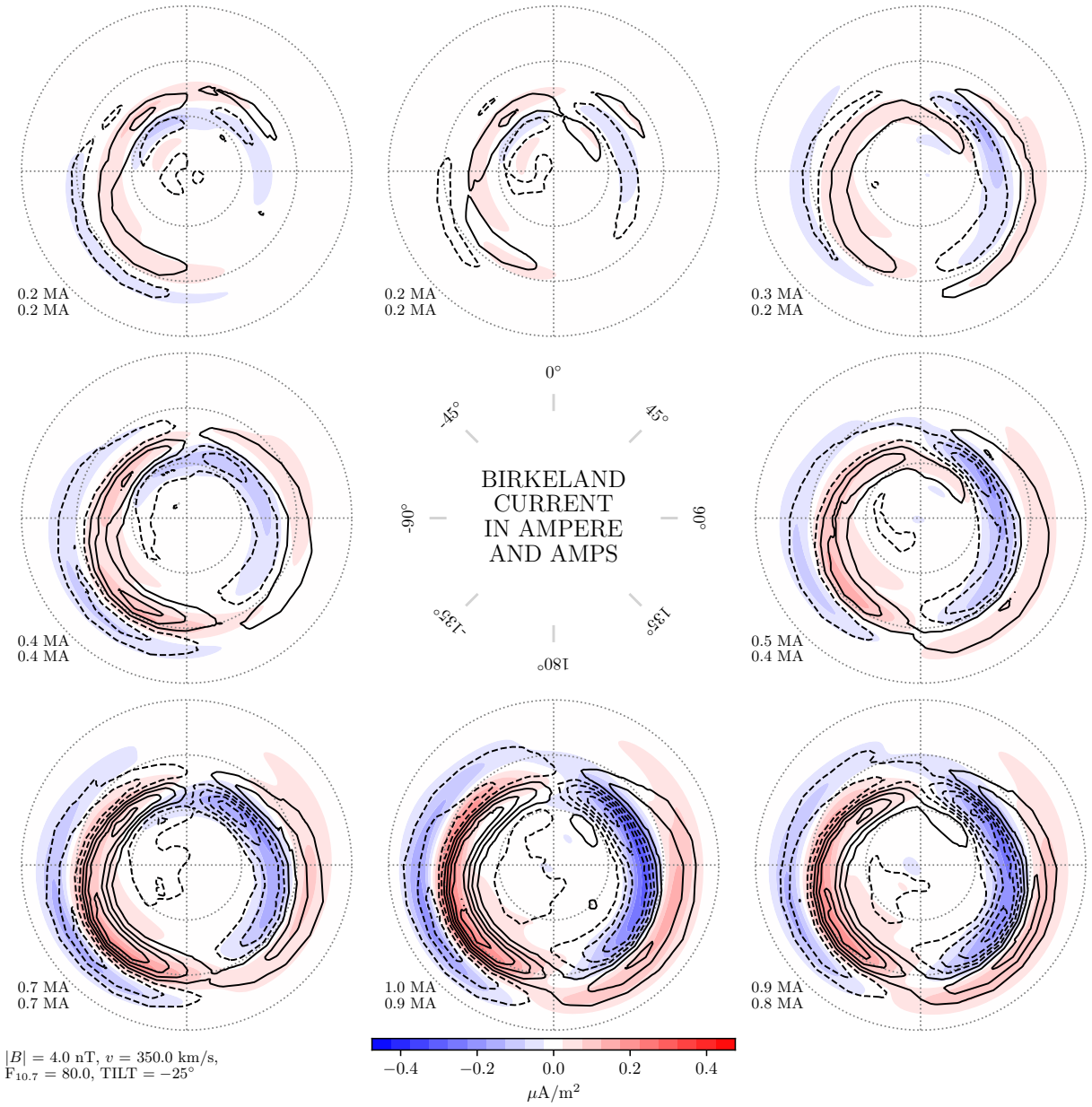

Figure 13: Maps of field-aligned current densities from the AMPS model (filled contours), for external conditions indicated in the lower left corner, and IMF orientation indicated in the center. The black contours show field-aligned current densities estimated with AMPERE, using bins defined by external conditions similar to values used with the AMPS model. The contour spacing is the same as in the filled contours, and dashed lines indicate negative (downward) current densities. The numbers in the lower left corners of each map shows the total upward current in AMPS (top) and AMPERE (bottom), in units of MA. The unit is given by the color scale below the maps. This plot corresponds to **winter** conditions (positive tilt) in the **north**ern hemisphere.

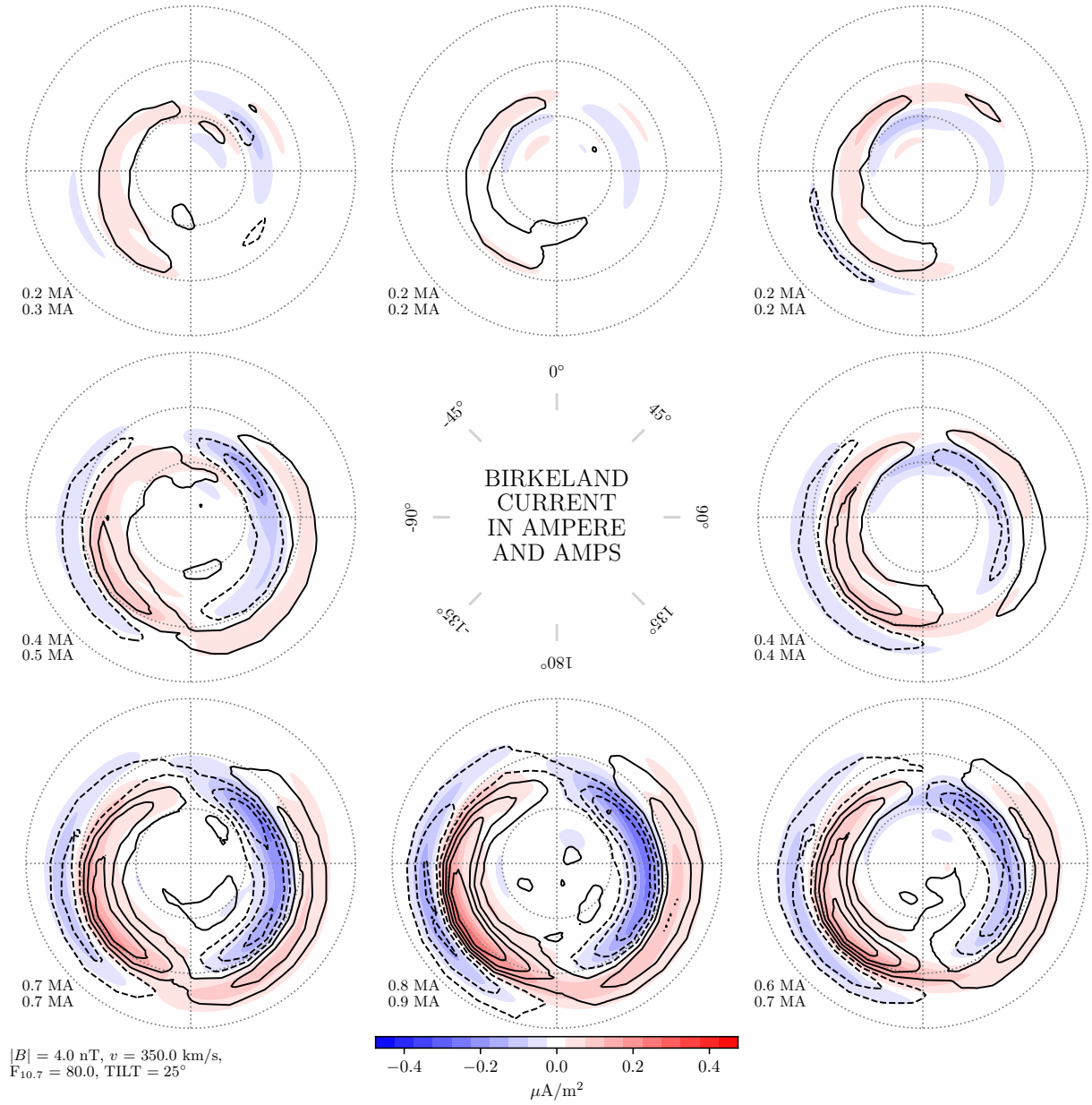

Figure 14: Maps of field-aligned current densities from the AMPS model (filled contours), for external conditions indicated in the lower left corner, and IMF orientation indicated in the center. The black contours show field-aligned current densities estimated with AMPERE, using bins defined by external conditions similar to values used with the AMPS model. The contour spacing is the same as in the filled contours, and dashed lines indicate negative (downward) current densities. The numbers in the lower left corners of each map shows the total upward current in AMPS (top) and AMPERE (bottom), in units of MA. The unit is given by the color scale below the maps. This plot corresponds to **winter** conditions (positive tilt) in the **south**ern hemisphere.

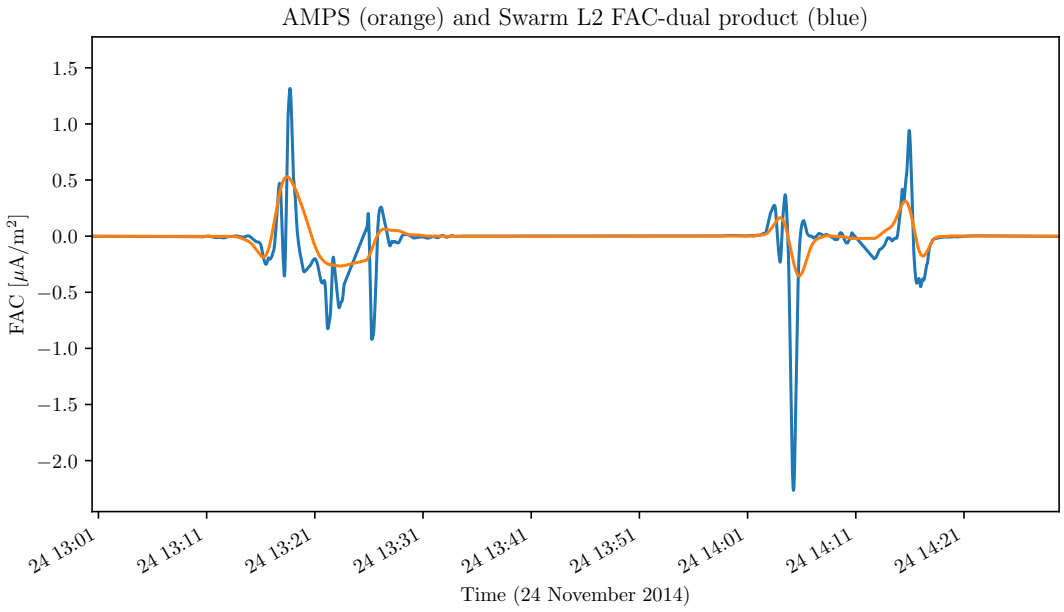

Figure 15: Example of AMPS model predictions of field-aligned current densities, and dual spacecraft estimates of FACs, using Swarm Alpha and Charlie. The latter is averaged over 30 s. The smooth orange curve represents AMPS field-aligned current estimates, and the blue curve represents the dual spacecraft estimates.

All quantities were calculated iteratively using Huber weights. We then separate each day in three classes of magnetic activity, defined by the daily average Ap index, using the 1/3 and 2/3 quantiles as limits. The median values for the comparison statistics in each group is shown in Figure 16.

Figure 16 shows that the correlation between AMPS and the dual spacecraft estimates of FACs is between 0.2 and 0.3. This is low, but significant. The prediction efficiency is negative, which means that AMPS predictions of dual spacecraft FACs are worse than using the mean value. The median slopes show that the AMPS FACs are on average 5-10% of the dual spacecraft estimates of FACs. All statistics decrease with increasing magnetic activity, but the decrease is more dramatic in the prediction efficiency.

In conclusion, we find that the correspondence between the FACs in the dual spacecraft estimates and in AMPS is poor. Based on the study by McGranaghan et al. [2017], this is not surprising. They find that the large-scale field-aligned current densities are not necessarily well correlated with small-scale current densities. Since the AMPS model describes the large-scale current densities, it should correlate better with the large-scale FAC estimates of AMPERE than with the small-scale FAC estimates from Swarm, as observed.

5 Comparison with ground magnetometers

The final comparison of this report is with ground magnetometer measurements. As in the previous section, we do not regard this comparison as entirely "fair", in that the AMPS model represents the magnetic field above the horizontal currents, and downward propagation to ground can only be performed with certain assumptions. The assumption that we make here is that the magnetic

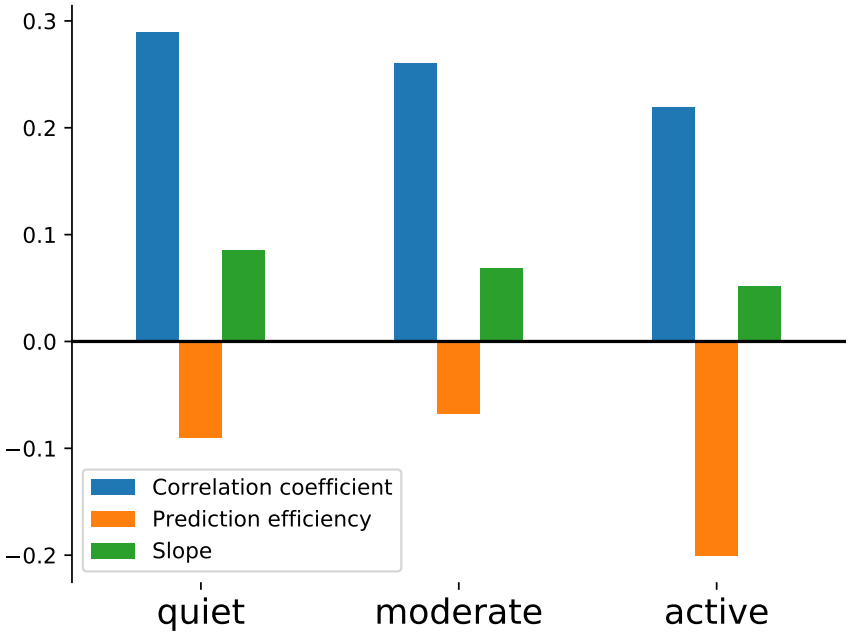

Figure 16: Medians of daily correlation coefficients, prediction efficiencies, and slopes comparing AMPS FAC estimates with dual spacecraft estimates of FACs. The means are calculated in three classes of magnetic activity, defined by the daily average Ap index, using the 1/3 and 2/3 quantiles as limits.

disturbance field on ground corresponds exclusively to an equivalent current at 110 km which equals the AMPS model divergence-free current at 110 km. In addition to the approximate selection of height, a key weakness with this approach is the omission of ground induced currents. Therefore, instead of focusing on direct comparison of magnetic field magnitudes, we investigate how the correspondence changes with time scales. The purpose of this is to substantiate our interpretation, that the AMPS model currents represents the part of the current which is associated with the direct solar wind driving.

The analysis in this section is based on comparisons between AMPS model values of the AL index and observed values between 1995 and 2015. To calculate model AL values, we first calculate the model magnetic field at the 12 AL station locations, and project the vector on the horizontal direction of the main magnetic field using the International Geomagnetic Reference Field (IGRF) model. The lower envelope curve, among the 12 stations, gives the model AL. We then compare model and observed AL index values at different time scales by applying a rolling average with different window sizes. Results are shown in Figure 17. We see that the correlation between the two time series increases with increasing window size, and reaches values close to 0.95 on time scales higher than $\sim$ 24 h. The root-mean-square misfit, which is calculated robustly with Huber weights, increases. This happens because the model increasingly underestimates the observations as the averaging window size increases.

The reason for this behavior may be explained by a fundamental property of the driving processes of polar ionospheric electrodynamics: The dayside coupling excites convection and currents, and this effect is largely described by the AMPS model. However, the dayside coupling also adds magnetic energy to the magnetospheric lobes, which is later explosively released in substorms, again exciting ionospheric currents. This delayed response, often called *unloading*, is not well described in the AMPS model. On short time scales, less than a couple of hours, the directly driven and unloading processes are poorly correlated [see e.g., Hubert et al., 2006], but they become very well correlated on long time scales. The reason for this is that over time, the opening of magnetic flux on the dayside and closure on the nightside must balance. Since the AMPS model is based on relatively high resolution data (1 Hz magnetic field measurements vs 20 min average solar wind data), the substorm signal will largely remain unmodeled noise. Averaged over time, however, the AMPS currents will be correlated with both the direct driving and unloading processes, but scaled only to the former. For this reason, it may be appropriate to introduce a scaling factor to the terms in the AMPS model that depend on dayside reconnection rate, ϵ (the Newell et al. [2007] coupling function).

Figure 18 shows the RMS misfit in model AL values vs. scale factor for the ϵ terms, for each of the averaging window sizes used in Figure 17. It shows that the optimal scale factor increases with window size, as expected. It also shows that the misfit decreases to less than 20 nT for window sizes larger than 24 h. Figure 19 shows the correlation and misfit statistics on the same format as in Figure 17, optimized with the scale factor found in Figure 18. It reveals that the decrease in misfit with the optimized AL index occurs on time scales between 1 and 24 hours, which corresponds to typical substorm cycle periods, and therefore the time scales where we might expect the dayside and nightside driving processes to become correlated. This result supports the interpretation that the AMPS model describes the currents and magnetic field disturbances associated with dayside solar wind driving.

The scale factors α determined in the AL comparisons are well described by the function

$$\alpha(\Delta T) = 1 + \frac{1.4}{1 + e^{-0.01(\Delta T - 14)}} \tag{2}$$

where ΔT is the averaging window size, in minutes. In Figure 20 we apply this scale factor

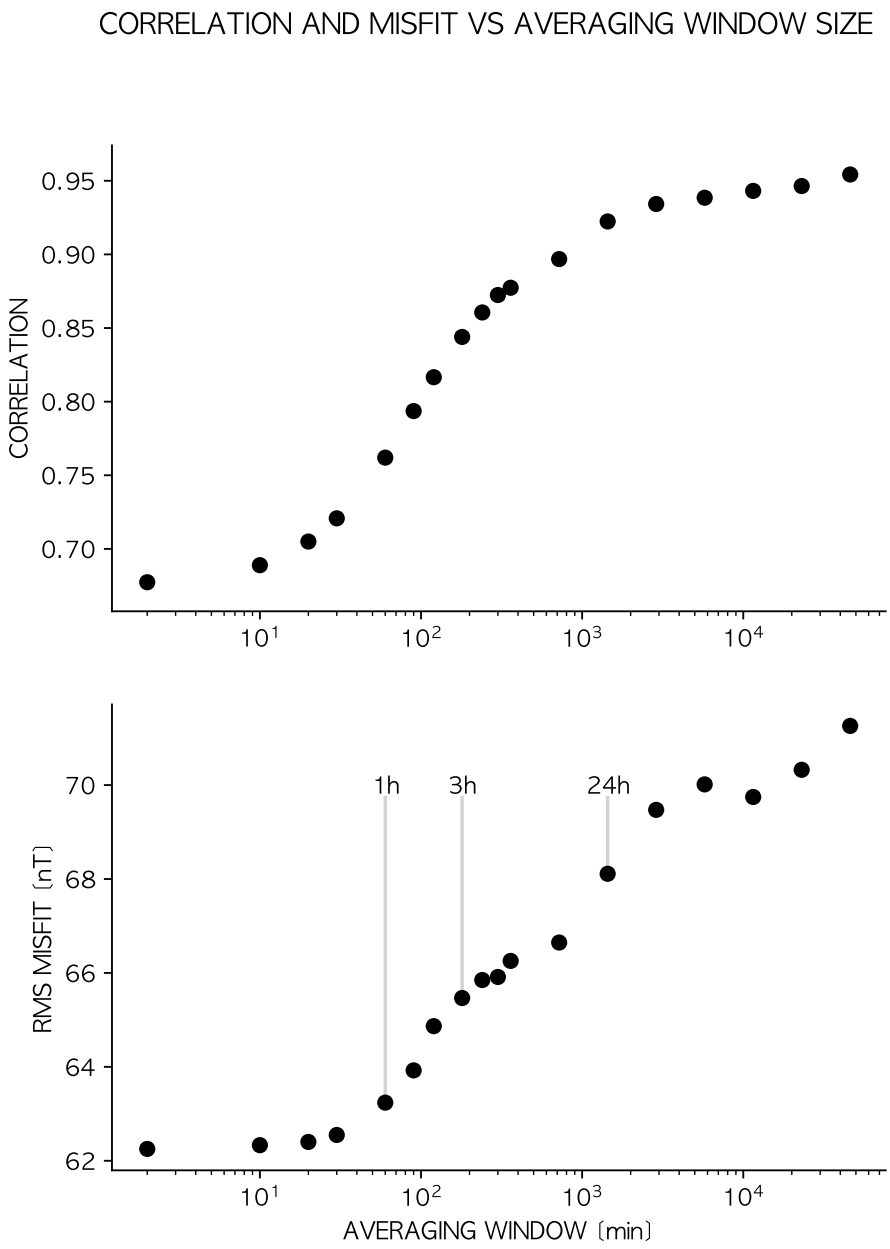

Figure 17: Top: Correlation coefficients between model AL index values and measured AL index values between 1995 and 2015 for different rolling window sizes, indicated at the x axis. Bottom: The root-mean-square misfit, calculated robustly, between measured and model AL indices, at different time scales.

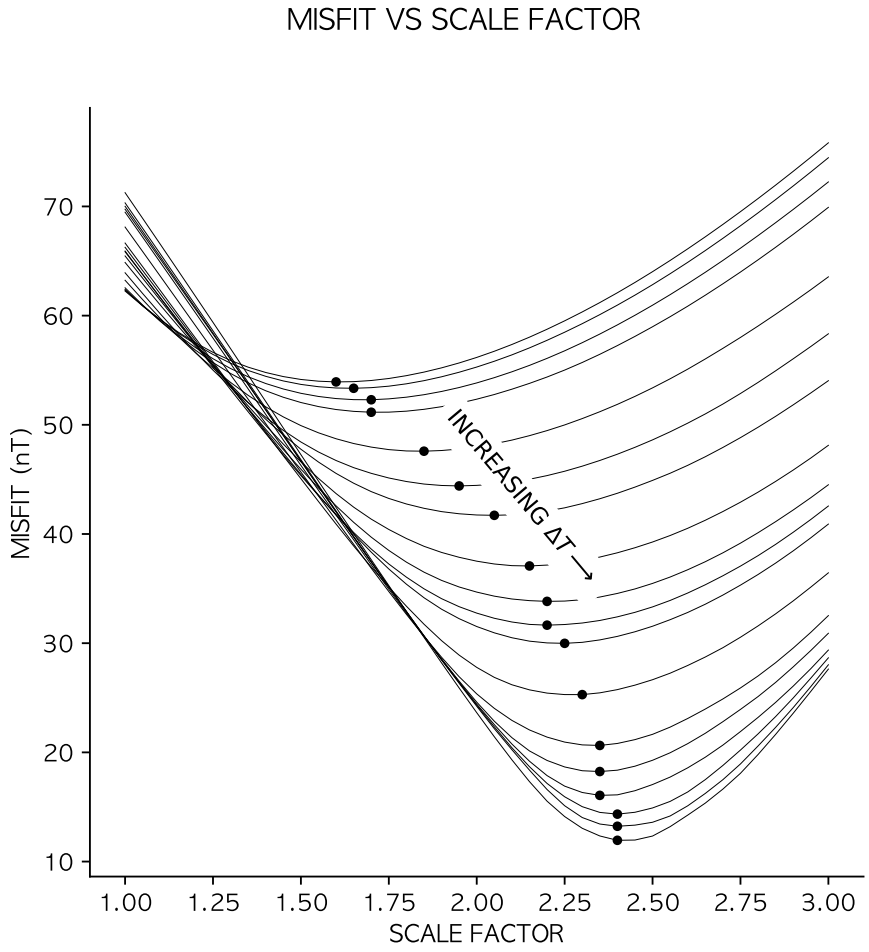

Figure 18: The RMS misfit vs. a scale factor for the terms of the AMPS model that are proportional to the ϵ parameter. The curves corresponds to the different time scales in the scatter plots in Figure 17. The minima of the curves are indicated by a black dot, and they decrease monotonically with increasing time scales.

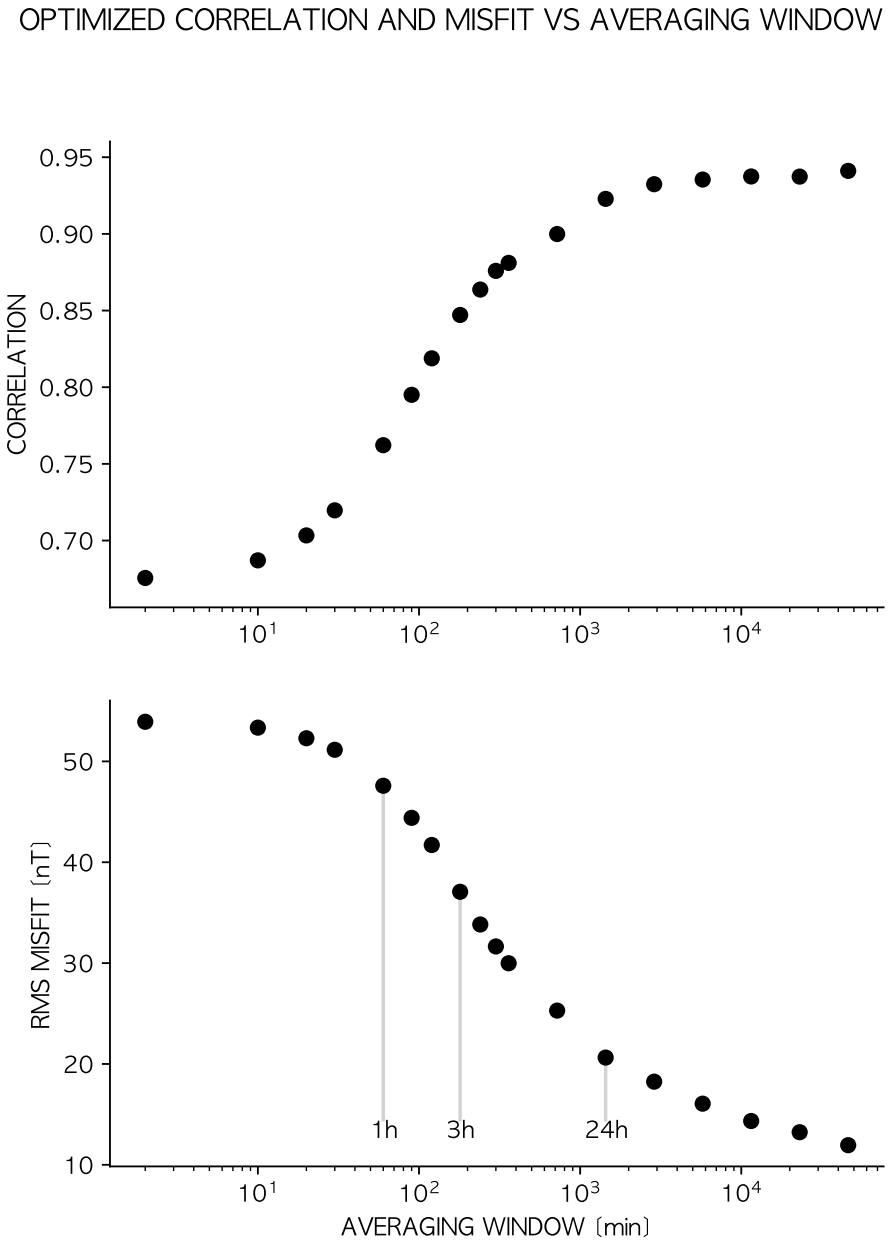

Figure 19: The format of this figure is the same as in Figure 17, but it is based on model AL index values that are optimized with the time scale dependent scale factors at the minima of the curves in Figure 18.

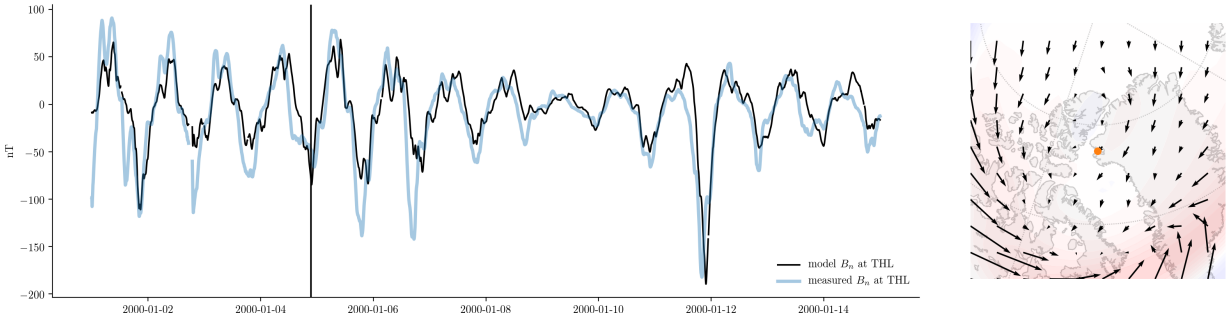

Figure 20: Left: 3-h average measured (blue) and modeled (black) northward magnetic field perturbation at Thule. Equation 2 has been used to scale the ϵ terms of the AMPS model. Right: A map of the surrounding AMPS current densities at the time indicated by the vertical black bar in the time series. Horizontal current densities are shown as black vectors, and field-aligned current densities are shown in color (red is up, blue is down).

when modeling the 3 h average northward magnetic component at the Thule magnetic observatory in Northern Greenland. The time series show modeled (black) and observed (blue) northward components. The map to the right shows the AMPS current system in the surrounding region at the time of the vertical bar in the times series. The good agreement in this figure indicates that the AMPS model can be useful for predicting slow variations in ground magnetic perturbations.

References

K. M. Laundal, C. C. Finlay, N. Olsen, and J. P. Reistad. Solar wind and seasonal influence on ionospheric currents from Swarm and CHAMP measurements. *J. Geophys. Res.*, 2018. doi: 10.1029/2018JA025387.

C. L. Waters, B. J. Anderson, and K. Liou. Estimation of Global Field Aligned Currents Using the Iridium System Magnetometer Data. *Geophys. Res. Lett.*, 28:2165–2168, 2001.

B. J. Anderson, K. Takahashi, and B. A. Toth. Sensing global Birkeland currents with Iridium engineering magnetometer data. *Geophys. Res. Lett.*, 27:4045–4048, 2000.

B. J. Anderson, H. Korth, D. T. Welling, V. G. Merkin, M. J. Wiltberger, J. Raeder, R. J. Barnes, C. L. Watersand A. A. Pulkkinen, and L. Rastaetter. Comparison of predictive estimates of high-latitude electrodynamics with observations of global-scale birkeland currents. *Space Weather*, 15 (2):352–373, 2017. doi: 10.1002/2016SW001529.

J. C. Coxon, S. E. Milan, J. A. Carter, L. B. N. Clausen, B. J. Anderson, and H. Korth. Seasonal and diurnal variations in AMPERE observations of the Birkeland currents compared to modelled results. *J. Geophys. Res.*, 2016. doi: 10.1002/2015JA022050.

S. E. Milan, J. S. Gosling, and B. Hubert. Relationship between interplanetary parameters and the magnetopause reconnection rate quantified from observations of the expanding polar cap. *J. Geophys. Res.*, 117, 2012. doi: 10.1029/2011JA017082.

P. Ritter, H. Lühr, and J. Rauberg. Determining field-aligned currents with the Swarm constellation mission. *Earth Planets Space*, 65:1285–1294, 2013. doi: 10.5047/eps.2013.09.006.

R. M. McGranaghan, A. J. Mannucci, and C. Forsyth. A comprehensive analysis of multiscale field-aligned currents: Characteristics, controlling parameters, and relationships. *Journal of Geophysical Research: Space Physics*, 122(12):11,931–11,960, 2017. doi: 10.1002/2017JA024742.

B. Hubert, , S. E. Milan, , A. Grocott, S. W. H. Cowley, and J. C. Gérard. Dayside and nightside reconnection rates inferred from IMAGE-FUV and Super Dual Auroral Radar Network data. *J. Geophys. Res.*, 111, 2006.

P. T. Newell, T. Sotirelis, K. Liou, C. I. Meng, and F. J. Rich. A nearly universal solar wind-magnetosphere coupling function inferred from 10 magnetospheric state variables. *J. Geophys. Res.*, 112, 2007. doi: 10.1029/2006JA012015.